A CAA Study of Turbulence Distortion in Broadband Fan Interaction Noise

Thomas Hainaut, Gwenael Gabard, Vincent Clair

A CAA Study of Turbulence Distortion in Broadband Fan Interaction Noise

Thomas Hainaut*, Gwénaël Gabard† and Vincent Clair‡

Institute of Sound and Vibration Research, University of Southampton, SO17 1BJ Southampton, UK.

The broadband noise generated by the interaction of the turbulent fan wakes on the outlet guides is a major noise source at approach conditions and its reduction is a challenge for turbofan engine manufacturers. In this paper, the linearized Euler equations are solved in the time-domain using a finite difference code to model the response of an isolated airfoil interacting with turbulence that is stochastically synthesized and injected in the computational domain through vorticity sources. The method of injection is firstly extended from one-component to two-component turbulence. The distortion of the turbulence by the mean flow near the leading edge is also investigated using this numerical method. Numerical simulations allow to collect simultaneously data for any variable and at any location in the computational domain, which is out of reach of experimental studies. So far, only a small number of numerical studies have been performed on this subject and were mainly focused on qualitative observations of turbulence. It has been found that, upstream the airfoil, the turbulence starts to decrease uniformly from a threshold distance independent of the wavenumber. At low frequency, this decay is however inverted after a second threshold distance, much closer to the leading edge, which is wavenumber dependent. A parametric study shows that the turbulence distortion is independent of the incoming turbulence, and that only the geometry forward the position of the maximum thickness has an effect on the distortion. It also shows that the nose radius, the position of the maximum thickness and maximum thickness of an airfoil affect the turbulence distortion. However, these geometric parameters alone are not sufficient to fully account for the distortion of the turbulence.

I. Introduction

At approach conditions, the thrust of turbofan engines is reduced making fan broadband noise a dominant source.[1] It can be decomposed into the self-noise of both the rotor and the guide vanes, the rotor-boundary layer interaction noise and the rotor wake-guide vanes interaction noise. This last component mainly contributes to broadband fan noise and is also referred as leading edge noise since the sources are concentrated at the leading edge of the vanes.

In numerical simulations, the presence of turbulence as well as the acoustic waves make simulations demanding in computational ressources. In the context of predicting broadband noise generated by the interaction of the turbulent wakes of the fan blades with the outlet guide vanes, one approach would be to consider the complete rotor-stator stage or an angular sector including one or more blade/vane channels. However, correctly modelling the turbulent wakes of the rotor would require solving the full governing equations, over a fine mesh, and the computational cost associated prevents the use of such method in an industrial context.

An alternative methodology consists in restricting the configuration to the stator only, and introducing a synthetic turbulence in the computational domain. This allows a drastic reduction in the size of the computational domain and, as the problem is limited to the study of the interaction of the injected turbulence with the stator, the generation and propagation of the noise can be obtained without solving the full governing equations. Nonetheless, the incoming turbulence has to be modelled and injected in the computational

*PhD student, t.hainaut@soton.ac.uk

†Associate professor, Senior member AIAA, gabard@soton.ac.uk

‡Research fellow, v.j.clair@soton.ac.uk

domain. This could be achieved by the use of stochastic methods, as introduced in 1970 by Kraichnan[2] where the fluctuating turbulent field is decomposed as a sum of Fourier modes. However, this summation can become computationally expensive as the number of modes increases. A second solution is to introduce eddies, calibrated to reproduce prescribed spatial and temporal correlations of the incoming turbulence, as proposed by Ewert *et al.*[3,4] in the Random Particle Method (RPM), by Dieste & Gabard,[5,6] by Jarrin*et al.*[7–9] or by Hainaut & Gabard.[10] This methodology allows to easily extract acoustic informations and to independently study the influence of each parameter of the simulation.

Leading edge noise has been studied by Dieste & Gabard[5,6,11] for a 2D flat plate at Mach 0.362 using a method similar to the RPM. They showed that the inclusion of the time decorrelation of the turbulence in the model has a very limited effect on the acoustic radiation of the flat plate. This might be explained by the fact that the turbulence has a relatively long correlation time compared to the time needed to convect along the flat plate. This observation indicates that generating a frozen turbulence should be satisfying to study interaction noise on an airfoil. Clair *et al.*[12] developed a specific stochastic model to generate a frozen turbulent velocity field from a sum of Fourier modes, taking inspiration from Amiet's model[13] to reduce the dimension of the model, and applied it to 3D airfoils. A similar method has also been developed by Gill *et al.*[14] to assess the effect of the airfoil thickness on the noise radiation.

The nose radius and thickness of the leading edge have a significant impact on the radiated noise as observed experimentally[15] or numerically.[16] It suggests that the distortion of the incoming turbulence by the mean flow close to the leading edge plays an important role in the radiated noise. Recently, Santana *et al.*[17] compared analytical predictions of the far-field sound generated by a turbulent field interacting with a NACA0012 airfoil by evaluating the distortion of the turbulence near the leading edge. The evaluation of the upwash turbulence is done using the modification proposed by Hunt[18] to the Rapid Distortion Theory (RDT)[19] and the modification of the turbulence enery spectum proposed by Christophe.[20] The RDT claims to describe the effect of the mean flow on the turbulence. The distortion is assumed to occur sufficiently rapidly so that the contribution to the change in relative position of fluid particles from the turbulence is negligible. Similarly, Glegg *et al.*[21] calculated the unsteady loading of an airfoil in incompressible turbulent flow using panel methods, and Lysak *et al.*[22] predicted the high frequency response using the vortex lift theory.[23]

Nevertheless, analytical methods developed to estimate interaction noise are restricted by assumptions made on the geometries and flow solution, and experimental studies are limited by technical difficulties to collect data. Therefore, numerical simulations seem to be an adequate solution as it is possible to record any variable at any location in the computational domain in the same simulation and at every time-step if necessary. Previous numerical studies[16,24] however mainly focused on qualitative observations such as the size of the stagnation region or the curvature of the streamline at the leading edge.

In this paper, the method developed to inject synthetic turbulence in a computational domain using localized vorticity sources[10] is extended from one-component to two-component turbulence. This method of injection has the advantages of being easy to implement and to parallelize in an existing solver, whilst the generated turbulence is frozen. Then, the distortion of the turbulence in the vicinity of the leading edge of a NACA0012-63 airfoil is studied. Finally, the distortion is analyzed through a parametric study on the main parameters of the simulations such as the mean flow velocity, the statistics of the turbulence and the geometry of the airfoil.

II. Synthetic turbulence injected through vorticity sources

The propagation of small amplitude perturbations on a mean flow can be described by the linearized Euler equations (LEE), written here in a non-conservative form:

$$\begin{cases} \dfrac{\partial \rho'}{\partial t} + \mathbf{u}_0 \cdot \nabla \rho' + \mathbf{u}' \cdot \nabla \rho_0 + \rho_0 \nabla \cdot \mathbf{u}' + \rho' \nabla \cdot \mathbf{u}_0 = 0 \ , & \text{(1a)} \\ \dfrac{\partial \mathbf{u}'}{\partial t} + (\mathbf{u}_0 \cdot \nabla)\mathbf{u}' + (\mathbf{u}' \cdot \nabla)\mathbf{u}_0 + \dfrac{\nabla p'}{\rho_0} - \dfrac{\nabla p_0 \rho'}{\rho_0^2} = \mathbf{S}_v \ , & \text{(1b)} \\ \dfrac{\partial p'}{\partial t} + \mathbf{u}_0 \cdot \nabla p' + \mathbf{u}' \cdot \nabla p' + \gamma p_0 \nabla \cdot \mathbf{u}' + \gamma p' \nabla \cdot \mathbf{u}_0 = 0 \ , & \text{(1c)} \end{cases}$$

where ρ, p, $\mathbf{u}$ and γ denote the density, pressure, velocity and specific heat ratio, respectively. The mean flow variables are denoted by the subscript $_0$ and the perturbation variables by the superscript $'$. The right-hand

side of the momentum equation $\mathbf{S}_v$ denotes a vorticity source. The LEE can be used as governing equations to study leading edge noise generation and acoustic wave propagation since they are able to support vortical, entropy and acoustic modes.[25]

In the present paper, the CAA solver PIANO (Perturbation Investigation of Aerodynamic NOise) developed by the DLR (German Aerospace Center) is used. It solves the LEE in the time domain using a 4^{th}-order DRP (Dispersion Relation Preserving) finite difference scheme with a 7-point stencil proposed by Tam & Webb,[26] which has been designed to minimize the numerical dispersion introduced by the discretization. The time integration is performed using a 4^{th}-order Runge-Kutta scheme with 4-stage. A 8^{th}-order selective filter is also applied in order to prevent high-frequency spurious oscillations to appear in the computational domain.

In this work, the synthetic turbulence is injected in the domain through localized vorticity sources. As mentioned before, the turbulent perturbations are then convected by the mean flow, leading to a frozen turbulent field.

We assume a vorticity source injected in a uniform mean flow, away from any other source, hence: $\rho' = 0$, $p' = 0$ and $\nabla \cdot \mathbf{u}' = 0$. Following those assumptions, one can simplify the LEE to obtain a transport equation:

$$\left(\frac{\partial}{\partial t} + u_0 \frac{\partial}{\partial x}\right) \mathbf{u}' = \boldsymbol{\mathcal{S}}_v(\mathbf{x}, t) \tag{2}$$

where the vorticity source term $\boldsymbol{\mathcal{S}}_v(\mathbf{x}, t)$ can be decomposed in a spatial distribution $\mathbf{g}(\mathbf{x})$ and a temporal signal $s(t)$ so that $\boldsymbol{\mathcal{S}}_v(\mathbf{x}, t) = \mathbf{g}(\mathbf{x}) s(t)$.

The spatial distribution of the vorticity source used in this paper is defined as the curl of a Gaussian vector potential $\boldsymbol{\psi}(\mathbf{x})$ which ensures divergence-free velocity perturbations and is defined as:

$$\mathbf{g}(\mathbf{x}) = \nabla \times \boldsymbol{\psi}(\mathbf{x}) = \nabla \times \left(Ab \sqrt{\frac{e}{\ln(4)}} \exp\left[-\ln(2) \frac{|\mathbf{x} - \mathbf{x}_c|^2}{b^2} \right] \mathbf{e}_z \right), \tag{3}$$

where b is the half-value radius of the Gaussian, A the amplitude, $\mathbf{x}_c = (x_c, y_c)$ the coordinates of the center of the Gaussian and $\mathbf{e}_z$ the axis of rotation.

The spatial Fourier transform of the spatial component will affect the frequency spectrum of the velocity fluctuations convected downstream of the source. Thus the frequency spectrum of the time component $s(t)$ injected through the local source has to be modified to ensure that the desired spectrum is obtained for the turbulence convected downstream of the source.

II.A. One-component turbulence

The frozen turbulence hypothesis implies $k_x = \omega / u_0$, hence the spectral density $S_{22}(k_x u_0)$ of the time signal $s(t)$ writes:[10]

$$S(k_x u_0) = \frac{|u_0|}{\pi^2} \frac{\Phi_{22}(k_x)}{|\hat{g}_2(k_x, y_c)|^2} \ , \tag{4}$$

where $\Phi_{22}(k_x)$ is the desired wavenumber spectrum of the fluctuating velocity component normal to the chord and $\hat{g}_2(k_x = \omega/u_0, y_c)$ is the Fourier transform of the spatial component of the source $\mathbf{g}(\mathbf{x})$, on the streamwise direction at the position $y = y_c$ defined in the following section.

Following the definition of the spatial distribution of the source given in equation 3, the evolution of the streamwise Fourier transform of the spatial component of the vorticity source $|\hat{g}_2(\omega/u_0, y)|$ in the normal-direction, at a given angular frequency ω_0, shows a Gaussian shape with a maximum at $y = y_c$. This means that the velocity field injected in the domain using the method presented in the previous section will fade away from $y = y_c$. It is possible to construct a spatial distribution of the source to keep a constant value of $|\hat{g}_2(\omega/u_0, y)|$, and thus of the velocity magnitude, over a chosen spatial extent in the normal-direction by superposing N_s evenly spaced Gaussian distributions. By doing so, the resulting energy is increased when setting multiple vorticity sources compared to a single source. A one-component turbulence implies that all the sources are coherent i.e. have the same temporal signal $s(t)$. To retain the same amount of energy, the amplitude parameter A can be corrected:

$$A = \left[2 \sum_{j=0}^{\infty} \exp\left(-\frac{\ln 2}{b^2} (jd)^2 \right) - 1 \right]^{-1} \ , \tag{5}$$

where d is the distance (in the transverse direction relative to the mean flow) between each source.

II.B. Two-component turbulence

To generate a two-component turbulence, the sources of vorticity have to be incoherent. However, if each temporal signal $s(t)$ is a different realization of the same spectral density $S(\omega)$, the resulting transverse wavenumber spectrum has a fixed shape given by the definition of the spatial distribution $\mathbf{g}$. Using the definition of $\mathbf{g}$ given in equation 3, it gives a Gaussian shaped spectrum. To control the wavenumber spectrum on both the streamwise and transverse direction, one solution is to sum lines of vorticity sources with different characteristics (i.e. half-radius and amplitude). The spatial distribution is assumed separable $g_i(x,y) = g_x(x)g_y(y)$ hence the spatial Fourier transform of $\mathbf{g}$ can be written as $\hat{g}_i(k_x,k_y) = \hat{g}_{ix}(k_x)\hat{g}_{iy}(k_y)$. As a result, the sum of N_l lines of vorticity sources where the subscript $(.)_l$ denotes the considered parameters (half-radius b_l and amplitude A_l) of each line source, leads the wavenumber spectrum $\phi_{ij}(k_x,k_y)$ to write:

$$\phi_{ij}(k_x,k_y) = \frac{2\pi^3}{|u_0|}\sum_l^{N_l} \hat{g}_{ix}(k_x,b_l)\overline{\hat{g}_{jx}(k_x,b_l)}\hat{g}_{jy}(k_y,b_l)\overline{\hat{g}_{iy}(k_y,b_l)}S_l(k_x u_0) \tag{6}$$

where $\hat{g}_i(k_x,k_y)$ is the forward Fourier transform on the x and y directions of the spatial distribution $g_i(x,y)$.

By definition, we have $\Phi_{22}(k_x) = \int_{\mathfrak{R}} \phi_{22}(k_x,k_y)\mathrm{d}k_y$ and $\Phi_{11}(k_y) = \int_{\mathfrak{R}} \phi_{11}(k_x,k_y)\mathrm{d}k_x$, hence, as for the one-component turbulence method, the spatial Fourier transform of the spatial component affects the frequency spectrum of the velocity fluctuations convected downstream of the source. Thus, for each source, the spectral density spectrum of the time component $s_l(t)$ has to be modified to ensure that the desired spectrum $\Phi_{22}(k_x)$ is obtained for the turbulence convected downstream of the source. One solution is to write:

$$S_l(k_x u_0) = a_l \frac{|u_0|}{2\pi^3}\frac{\Phi_{22}(k_x)}{|\hat{g}_{2x}(k_x,\lambda_l)|^2\int_{\mathfrak{R}}|\hat{g}_{2y}(k_y,\lambda_l)|^2\mathrm{d}k_y}\ , \qquad \text{with}\ \ \sum_l^{N_l} a_l = 1\ . \tag{7}$$

It directly follows the wavenumber velocity spectrum $\Phi_{11}(k_y)$ to write:

$$\Phi_{11}(k_y) = \sum_l^{N_l} a_l \frac{|\hat{g}_{1y}(k_y,\lambda_l)|^2}{\int_{\mathfrak{R}}|\hat{g}_{2y}(k_y,\lambda_l)|^2\mathrm{d}k_y}\int_{\mathfrak{R}}\Phi_{22}(k_x)\frac{|\hat{g}_{1x}(k_x,\lambda_l)|^2}{|\hat{g}_{2x}(k_x,\lambda_l)|^2}\mathrm{d}k_x\ . \tag{8}$$

To ensure that the sources correctly interfere with each other, the sources need to be close enough. It has been found empirically that the distance d between each source (in the transverse direction relative to the mean flow) should respect $d \leq 0.9b_l$. Moreover, to retain the same amount of energy, the amplitude parameter A_l should be corrected:

$$A_l = \sqrt{\frac{b_l}{\sqrt{2\ln 2}}\sqrt{\pi}\left[2\sum_{j=0}^{\infty}\exp\left(-\frac{2\ln 2}{b_l^2}(jd_l)^2\right)-1\right]^{-1}}\ . \tag{9}$$

II.C. Construction of the time signal $s(t)$

For the one- and two-component turbulence, the method relies on the generation of a time signal $s(t)$ which respects the given spectral density $S(\omega)$. Several methods has been proposed in the literature for this purpose, for instance for generating non-Gaussian signals,[27] or using wavelets.[28] The method used here is based on a Fourier transform[29] where the time series $s_n = s(t_n)$ is related to its discrete Fourier transform $\hat{s}_m$ through:

$$s_n = \frac{1}{N}\sum_{m=0}^{N-1}\hat{s}_m \mathrm{e}^{2\pi \mathrm{i}mn/N}, \qquad \text{with}\ \hat{s}_m = \sqrt{2\pi N^2 \Delta f S(\omega_m)}\mathrm{e}^{+\mathrm{i}\phi(\omega_m)}\ , \tag{10}$$

where the magnitude of the Fourier coefficients $\hat{s}_m$ are defined to match the power spectral density S, and the phase ϕ associated with each discrete frequency ω_m is randomly generated between 0 and 2π using a uniform probability distribution, with the additional constraint that $\phi(-\omega_m) = -\phi(\omega_m)$ to obtain a real-valued signal.

Finally, the resulting discrete temporal signal $s_n = s(t_n)$ is used to form the vorticity source $\boldsymbol{\mathcal{S}}_v(\mathbf{x},t_n) = \mathbf{g}(\mathbf{x})s(t_n)$.

II.D. Validation of the method

The presented method to inject frozen two-component turbulence using sources of vorticity is validated in a free-field uniform mean flow simulation. The one-component turbulence has already been validated.[10] The computational domain extends between $0 \leq x \leq 7$ and $-5 \leq y \leq 5$. The domain is discretized with a uniform spacing $\Delta x = \Delta y = 0.02$. The non-dimensionalized variables of the problem are the static density $\rho^*_\infty = 1$, the static speed of sound $a^*_\infty = 1$ and a length $L^* = 1$. The mean flow velocity is uniform, oriented in the x-direction, with a Mach number $M = 0.5$. Tam outflow boundary condition[26] is used on the downstream boundary, and Tam radiation boundary condition[26] on the others. The non-dimensionalized time step is set to $t^* = 0.012$, which gives a CFL number of 0.9, and the simulation is run over 2^{18} iterations. Such a large number of iterations is used for validation purposes, to average the wavenumber spectrum on multiple segments by performing a periodogram. To prevent spurious oscillations to develop in the domain, a 8^{th}-order explicit filter is applied at every time step.

The vorticity sources are evenly spaced on a line, normal to the mean flow, at $x = 1.5$ from $y = -3.5\ m$ to $3.5\ m$ and 300 velocity sensors located at $x = 6.5$ from $y = -3\ m$ to $3\ m$ record the velocity fluctuations as the gusts convect.

The incoming turbulence $\Phi_{22}(k_x)$ is modeled by a one-wavenumber von Karman spectrum, using a turbulent integral length scale $\lambda = 0.1\ m$ and the turbulence intensity $T_I = \sqrt{\overline{u_2'}^2/u_\infty^2} = 2.5\%$, can be expressed by:

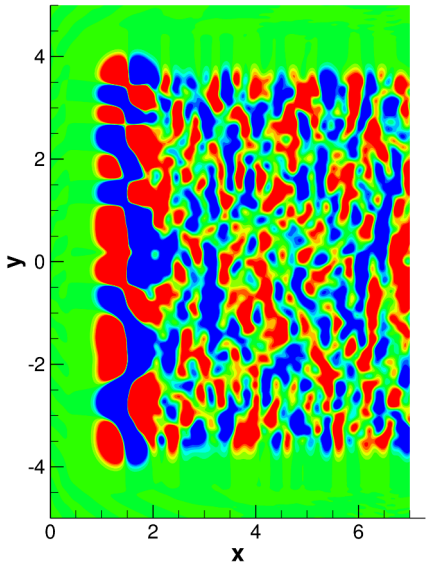

Figure 1: Instantaneous transverse velocity fluctuations plotted between $u_2^{'*} \pm 0.01$.

$$\Phi_{22}(k_x) = \frac{\overline{v'^2}\lambda}{6\pi}\frac{3+8\tilde{k}_x^2}{\left[1+\tilde{k}_x^2\right]^{11/6}} \quad ; \quad \tilde{k}_x = \frac{k_x}{k_e} \quad ; \quad k_e = \frac{\sqrt{\pi}}{\lambda}\frac{\Gamma(5/6)}{\Gamma(1/3)}\ , \tag{11}$$

where $\Gamma(.)$ is the gamma function. The discretization of the spectrum is realized between $k_{x_{\min}} = 2$ to $k_{x_{\max}} = 20$. For the wavenumber velocity spectrum $\Phi_{11}(k_y)$, three different set of sources are used.

The instantaneous y-velocity fluctuation is plotted in Figure 1. It shows the turbulence generated at the vorticity source locations, on the desired y-extent and convected downstream by the uniform mean flow. Moreover, the solution does not seem to be contaminated by reflections on the downstream boundary.

The turbulence is frozen, hence using the relation $S_{\text{sensor}}(\omega = ku_0) = \Phi_{22}(k_x)/u_0$, the measurement of the instantaneous velocity perturbations from one sensor allow the computation of the turbulence velocity spectrum $\Phi_{22}(k_x)$ in the simulations. The spectral density of the turbulent velocity is calculated using a Welch method with 80 segments and an overlapping of 10%. It allows a reduced noise in the estimated power spectrum in exchange for reducing the frequency resolution, compared to standard periodogram methods. On the other hand, the velocity spectrum $\Phi_{11}(k_y)$ is computed from the two-point correlation R_{ij} calculated using the unsteady values of the sensors. The velocity spectrum $\Phi_{11}(k_y)$ and $\Phi_{22}(k_x)$ derived from the two simulations are plotted in Figure 2. It shows a good agreement in terms of frequency limits and amplitudes between the prescribed and simulated spectra.

III. Distortion of the turbulence

The nose radius and thickness of the leading edge have a significant impact on the radiated noise as observed experimentally[15] or numerically.[16] It suggests that the distortion of the incoming turbulence by the mean flow close to the leading edge plays an important role in the radiated noise. Recently, Santana *et al.*[17] compared analytical predictions of the far-field sound generated by a turbulent field interacting with a NACA0012 airfoil by evaluating the distortion of the turbulence near the leading edge. The evaluation of

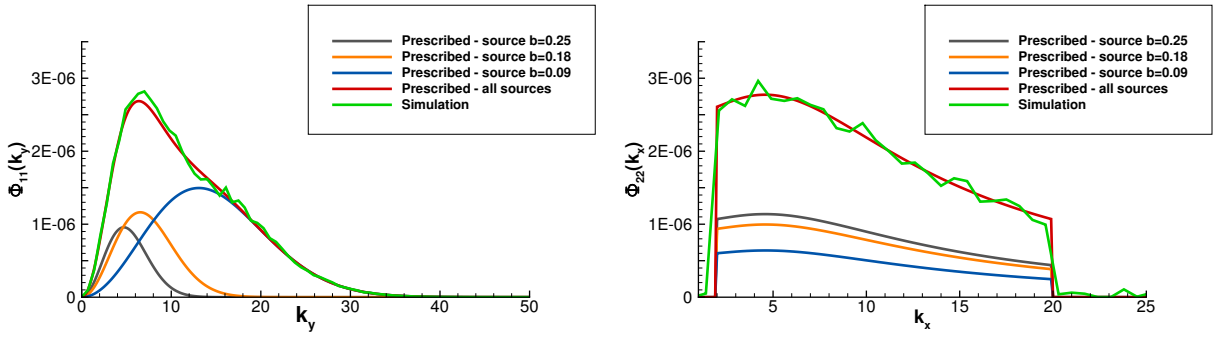

(a) $\Phi_{11}(k_y)$ (b) $\Phi_{22}(k_x)$

Figure 2: Plots of the measured velocity spectrum against the prescribed velocity spectrum.

the upwash turbulence is done using the modification proposed by Hunt[18] to the Rapid Distortion Theory (RDT)[19] and the modification of the turbulence enery spectum proposed by Christophe.[20] The RDT claims to describe the effect of the mean flow on the turbulence. The distortion is assumed to occur sufficiently rapidly so that the contribution to the change in relative position of fluid particles from the turbulence is negligible. Similarly, Glegg *et al.*[21] calculated the unsteady loading of an aerofoil in incompressible turbulent flow using panel methods, and Lysak *et al.*[22] predicted the high frequency response using the vortex lift theory.[23]

Nevertheless, analytical methods developed to estimate interaction noise are restricted by assumptions made on the geometries and flow solution, and experimental studies are limited by technical difficulties to collect data. Therefore, numerical simulations seem to be an adequate solution as it is possible to record any variable at any location in the computational domain in the same simulation and at every time-step if necessary. A small number of numerical studies[16,24] already looked at the distortion, but they only focused on qualitative observations such as the size of the stagnation region or the curvature of the streamline at the leading edge.

III.A. Setup

To study the distortion of the turbulence in the vicinity of the leading edge, a symmetric NACA0012-63 profile is first considered. The chord of the airfoil is $c = 0.1$ m, at no angle of attack and the incoming free stream velocity is $u_\infty = 60$ m.s^{-1}.

The choice of a modified NACA 4-series airfoil is motivated by the possibility to independently control the size of the leading edge radius R_{LE}, the thickness t and the chordwise position of maximum thickness m (in tenths of chord). Indeed, usual NACA 4-series define the maximum thickness to be at a fixed location of 30% of the chord, and the leading edge radius to be directly proportional to the square of the thickness ($R_{\text{LE}} \propto t^2$). The symmetric modified NACA four-series profiles are written as:[30]

$$\text{NACA } 00 \underbrace{12}_{t} - \underbrace{6}_{I} \underbrace{3}_{m},$$

where I is the leading edge index which directly relates to the size of the nose radius, and is given by:[30]

$$R_{\text{LE}} = \frac{1.1019}{36}\left(\frac{t}{c} * I\right)^2, \tag{12}$$

As the mean flow defines the streamlines along which the velocity fluctuations are convected, a correct estimation is required. However, in a CAA simulation, the presence of shear layers, boundary layers or significant velocity gradients can be a source of linear instabilities in the LEE. In this work, a steady Euler solver has been chosen to estimate the mean flows. A steady Euler assumes an ideal fluid with no viscosity, hence there is no physical boundary layers on the airfoil as the flow slips on the surfaces. It makes CAA computations more stable while being satisfactory to study broadband interaction noise.[10,14] Moreover, the computational domain for the mean flow simulation is sufficiently large to limit blockage effects (blockage ratio of 3%).

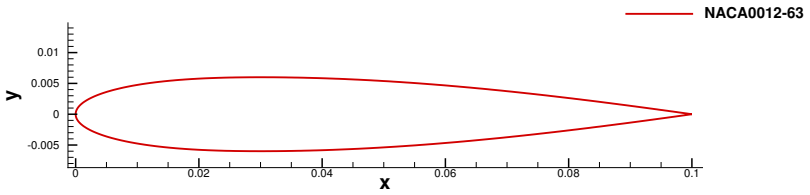

Figure 3: NACA0012-63

The CAA mesh is organized in a C-mesh configuration, with a extent of $x = -0.5$ to 0.6 m and $y = \pm 0.5$ m and is divided in 64 blocks to allow a parallelization of the computation. It has been designed to support hydrodynamic and acoustic waves up to 8kHz, considering 12 points per wavelength, for mean flow velocities ranging from 60 m/s to 140 m/s. The acoustic waves are supported everywhere in the domain while the hydrodynamic waves are only supported upstream the airfoil, on a limited y-extent, to convect the turbulent gusts. To prevent unwanted reflections at the boundaries, Tam's radiation boundary condition[26] is applied on the upstream, top and bottom boundaries of the computational domain, and Tam's outflow boundary condition[26] on the outflow boundary. These boundaries conditions are derived from asymptotic solutions of the linearized Euler equations to let acoustic waves leave the domain while minimizing reflections. The outflow boundary condition also allows hydrodynamic structures to exit the domain. Downstream the airfoil, the small hydrodynamic structures are slowly dissipated by the mesh before reaching the outflow boundary.

The computation is non-dimensionalized using the chord of the airfoil $c = 0.1$ m, the static speed of sound $a_\infty = 340$ m/s and the static density $\rho_\infty = 1.2$ kg/m^3. The non-dimensionalized time step of the simulation is $4.8.10^{-5}$, corresponding to a maximum local CFL number of 0.9 at the leading edge.

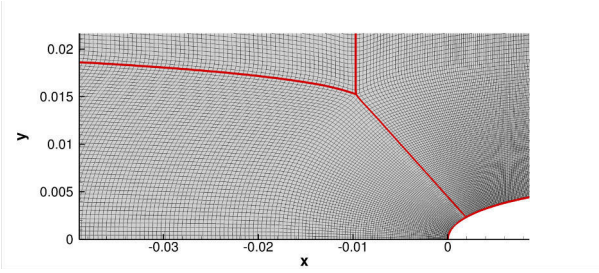

Figure 4: Mesh (black) and blocks (red).

The turbulence is injected through vorticity sources located upstream of the airfoil, at a distance $x = -2c$ from the leading edge, where the mean flow is feebly non-uniform. As discussed earlier, a row of vorticity sources is set to generate a turbulence with a constant amplitude over a specific distance in the direction normal to the streamlines. Two cases have been considered, a one- and two-component turbulence. The statistics of the turbulence respect a one-wavenumber von Karman spectrum with an integral length scale $\lambda = 8\ mm$ and a turbulent intensity $T_I = \sqrt{\overline{v'}^2/u_\infty^2} = 1.7\%$.

III.B. Far-field radiation

To estimate the response of the airfoil in the far-field while limiting the size of the computational domain, a Ffowcs-Williams & Hawkings analogy in the frequency domain[31,32] is used. This is an exact rearrangement of the general Navier-Stokes equations with the assumption that the source region is limited within a control surface. It simplifies to a convected wave equation with equivalent sources located on the control surface that will generate the same acoustic field as if the full Navier-Stokes equations were solved. These equivalent sources are separated into monopole Q, dipole F and quadripole T terms. If the control surface contains all the acoustic sources, the quadripole term can be neglected. Assuming that the control surface is in a uniform translated motion, the integral form of the analogy in the spectral domain can be written:[31,32]

$$\hat{p}(\mathbf{y},\omega) = \iint_S i\omega \hat{Q}_n(\mathbf{x},\omega)\hat{G}(\mathbf{y},\omega|\mathbf{x})\,\mathrm{d}S + \iint_S \hat{F}_i(\mathbf{x},\omega)\frac{\partial \hat{G}(\mathbf{y}|\mathbf{x},\omega)}{\partial x_i}\,\mathrm{d}S \tag{13}$$

with $\mathbf{y}$ the location of the observer and $\mathbf{x}$ the points on the control surface S. $\hat{G}(\mathbf{y}|\mathbf{x},\omega)$ is the 2D free-field Green function in the spectral domain for a uniform mean flow in the x-direction, defined as:

$$\hat{G}(\mathbf{y}|\mathbf{x},\omega) = \frac{i}{4\beta}H_0^{(2)}\left(\frac{kS_0}{\beta^2}\right)\mathrm{e}^{\frac{ikM}{\beta^2}(y_1-x_1)} \tag{14}$$

with $S_0 = \sqrt{(y_1 - x_1)^2 + \beta^2 (y_2 - x_2)^2}$, $\beta^2 = 1 - M^2$ and $H_0^{(2)}(.)$ the Hankel function of the second kind and 0^{th} order. The control surface S has outwards normals $\mathbf{n}$.

- $Q_n = \left[(\rho_0 + \rho')(u_{0i} + u_i') - \rho_0 u_{0i}\right] n_i$ represents the monopolar contribution,
- $F_i = \left[(p_0 + p')\delta_{ij} + (\rho_0 + \rho')(u_i' - u_{0i})(u_{0j} + u_j') + \rho_0 u_{0i} u_{0j}\right] n_j$ represents the dipolar contribution.

The source terms are calculated in the time domain, and then a Fourier transform is applied to the groupings Q_n and F_i. Moreover, the steady components do not propagate to the far-field and the acoustic propagation is assumed to be linear, hence it can be reduced to $Q_n = \left[\rho_0 u_i' + \rho' u_{0i}\right] n_i$ and $F_i = \left[p'\delta_{ij} + (\rho_0 u_i' - \rho' u_{0i})\, u_{0j} - \rho_0 u_{0i} u_j'\right] n_j$.

III.C. Instantaneous and acoustic results

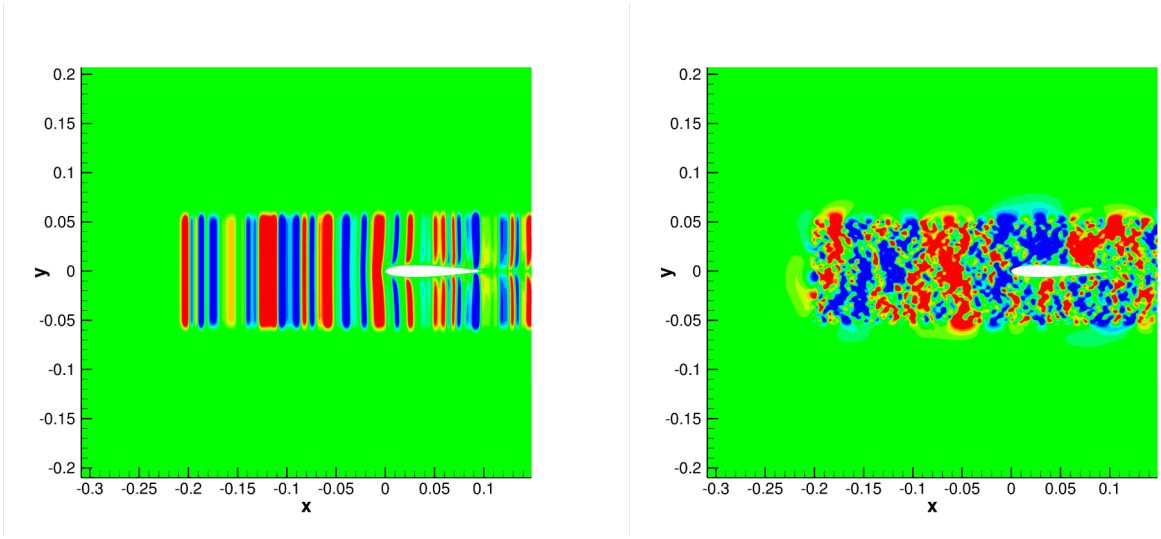

(a) One-component turbulence.

(b) Two-component turbulence.

Figure 5: Instantaneous transverse velocity perturbation contour between $\pm 1 m.s^{-1}$.

After the transitional period, the computations are run over 2^{18} iterations, taking about 2 hours on 64 Intel Xeon E5-2670 processor cores. The instantaneous normal-velocity perturbaturbations for the one- and two-component turbulence are presented in Figure 5. We can observe the turbulent gusts generated upstream of the profile, in between the inlet boundary and the leading edge, with a limited extent in the y-direction, and being convected by the mean flow. The pressure fluctuations, plotted in Figure 6a, show an expected dipolar pattern of the acoustic response of the airfoil. Moreover, the pressure fluctuations does not seem to show spurious reflections at the Tam boundary conditions, which would contaminate the solution.

A set of 720 equally spaced sensors are located on a circle centered on the leading edge, with a radius of four chords, to record the perturbations and perform the FWH analogy (described in section III.B). The numerical predictions are compared with the analytical results of the Amiet model which considers a flat plate.[13] Figure 6b shows the Sound Pressure Level (SPL) at 1.2m and 90°(above the airfoil), along with the Amiet model prediction. The spectra are averaged on 15 segments using a Hann window and an overlapping of 50%. The low-frequency part of the acoustic spectrum is similar to a flat plate response, as the wavelength is greater than the chord of the profile. But as the wavelength shortens, it becomes more sensitive to the airfoil geometry (and by extension to the mean flow), which implies a different acoustic response compared to a flat plate at high frequencies.

III.D. Streamline to the stagnation point

The reduction in the SPL at high frequencies is due to the distortion of the mean flow in the vicinity of the leading edge. To better understand this phenomenon, a line of sensors is placed on a streamline which starts upstream the profile and stops to the stagnation point of the leading edge. As the studied profile is

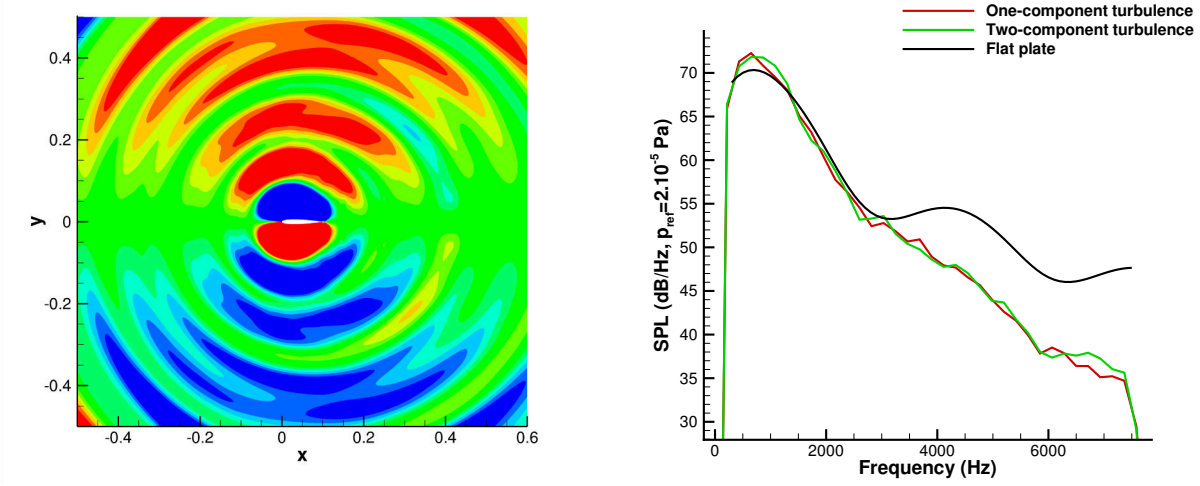

(a) Instantaneous pressure perturbation contour between ±4Pa. (one-component turbulence).

(b) SPL at 90°and R=1.2m above the airfoil.

Figure 6: Acoustic response of a NACA0012-63.

symmetric, it corresponds to a line parallel to the x-axis with y = 0 m, as plotted on Figure 7a, along with the mean pressure field.

The turbulence is frozen, hence using the relation $S_{\text{sensor}}(\omega = k_x u_0) = \Phi_{22}(k_x)/u_0$, the measurement of the instantaneous velocity perturbations from the sensors allow the computation of the turbulence velocity spectrum $\Phi_{22}(k_x)$ at the different locations in the simulations. The spectral density of the turbulent velocity is calculated using a Welch method over multiple segments which allows a reduced noise in the estimated power spectrum in exchange for reducing the frequency resolution, compared to standard periodogram method.

The observation of the velocity spectra $\Phi_{22}(k_x)$ at different locations upstream the airfoil shown on Figure 7b depicts the following behavior:

- No distortion is occurring far from the airfoil.
- At a threshold distance common to all frequencies, around half a chord upstream, the levels of $\Phi_{22}(k_x)$ start to decrease uniformly independently of the wavenumber.
- At low frequency, this decay is however inverted after a second threshold distance which depends on the wavenumber, or in other words, it is proportional to the hydrodynamic wavelength (ω/u_{inf}). The lower the wavenumber, the greater this second distance is.

The Figures 8a and 8b plot the distortion of the turbulence at different frequencies as a function of the distance to the leading edge multiplied by the wavenumber of the frequency considered. The Figure 8a is a colormap which contains all the frequencies, and the Figure 8b is the same graph but only plotted for 4 fixed frequencies (ranging from low to high-frequency). On these figures, the second threshold is clearly visible and confirms that the distortion is wavenumber-dependent. Nevertheless, we observe that the tendancy which increases the levels of $\Phi_{22}(k_x)$ from the second threshold distance is less important as the frequency increases, to become inexistent at high frequency. We can also note that, on the closest points to the profile, the increase of the low frequencies of the spectrum $\Phi_{22}(k_x)$ gives greater levels than the turbulence injected initially. Nevertheless, this increase does not lead to an increase of the radiated noise at low frequencies when the far-field spectrum is compared to a flat plate where no turbulence distortion occurs. as visible on Figure 6b.

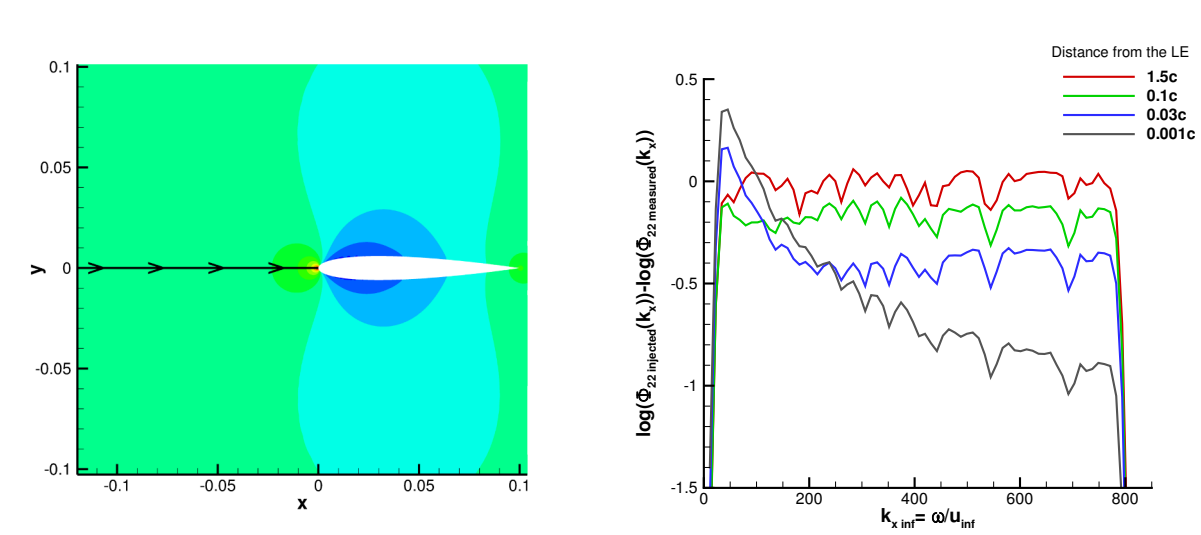

(a) Colormap of the mean pressure field around the airfoil along the streamline with stops to the stagnation point.

(b) Wavenumber velocity spectrum $\Delta\Phi_{22}(k_x)$ measured at different locations upstream the airfoil.

Figure 7: Streamline which stops at the stagnation point, and wavenumber velocity spectrum $\Delta\Phi_{22}(k_x)$ measured at different locations on this streamline.

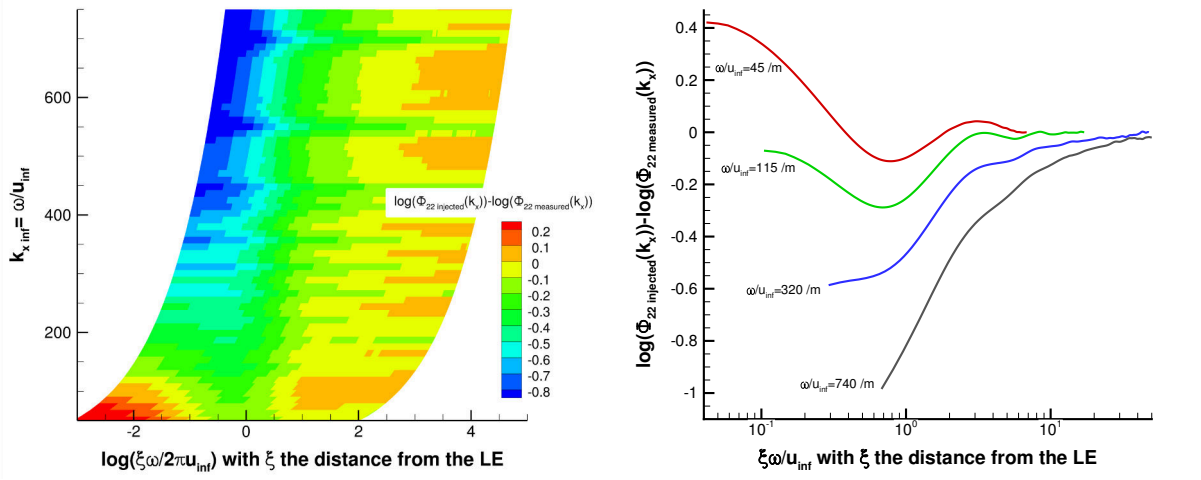

(a)

(b)

Figure 8: Distortion of the turbulence at different frequencies as a function of the distance to the leading edge multiplied by the wavenumber of the frequency considered.

IV. Parametric study of the distortion

To better understand the distortion of the turbulence, a parametric study is performed on the main parameters of the simulation. This includes the effects of the mean flow velocity, the incoming turbulent gusts, and some geometric effects.

IV.A. Effect of the mean flow velocity

In this section, the effect of the mean flow velocity is investigated. Velocities from 60 to 140 m/s have been considered, with a increment of 20 m/s. The geometry used is a NACA0012-63 and the incoming turbulence gusts respect a von Karman spectrum with a integral length scale IS=8mm and a turbulent intensity of 1.7%.

The same mesh has been used for all simulations, yet the time-step has been adjusted for each simulation to keep a CFL close to unity, speeding up the simulations.

The Sound Power Level (PWL) integrated over 360°of each simulation is plotted on Figure 9a. It shows the same slope when plotted as a function of ft/u_∞, as previously observed.[15] Hence the noise reductions follow a Strouhal dependence $\Delta\text{PWL}(l_{\text{efficient}}/u_\infty)$ where $l_{\text{efficient}}$ would be an appropriate length-scale based on the geometry of the airfoil. Hence, it would suggests that the distortion has a similar behavior for each wavenumber $k_x = 2\pi f/u_\infty$, which is confirmed to some extent by the plot of the evolution of $\Phi_{22}(k_x)$ on Figure 9b. The location of the first and second threshold distances which starts to decrease the spectrum $\Phi_{22}(k_x)$ uniformly for the first one and inverse the decay at low frequencies for the second, is shifted toward the leading edge as the mean flow velocity is increased. Moreover, at any fixed wavenumber, a small change in the slope between the different velocities can be perceived. These differences could be partly due to compressibility effects.

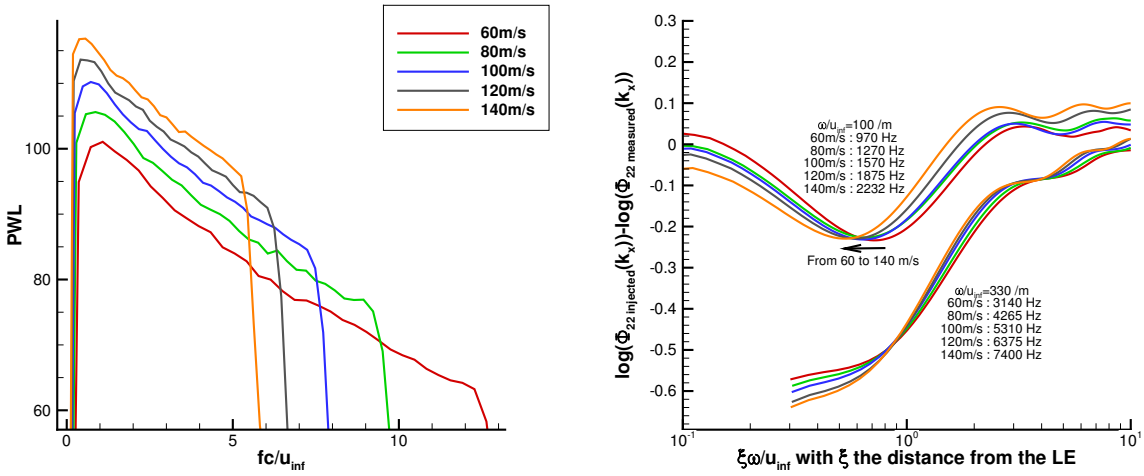

(a) Sound Power Level (PWL).

(b) Distortion of $\Phi_{22}(k_x)$.

Figure 9: Sound power level and distortion of the turbulence at different mean flow velocities.

IV.B. Effect of the incoming turbulence

In this study, the turbulence is considered isentropic and follows a von Karman energy spectrum, hence it can be fully characterized by a turbulent intensity and an integral length scale. The evolution of the spectrum with the turbulent intensity is linear, therefore easy to predict, whereas a change of the integral length scale leads to change the rate of the energy decay. In this section, the impact of the integral length scale on the distortion of the turbulence and on the noise radiated is studied using three different values: 0.004 m, 0.008 m and 0.012m.

Following Amiet's model[13] for a flat plate, the chord-wise integral of the surface loading of a flat plate with a chord c and a span $2d$ is defined as:

$$\mathcal{L}(x, K_x, k_y) = \int_{-c/2}^{c/2} g(x, K_x, k_y) \mathrm{e}^{-i\omega x_0 (M - x/\sigma)/a_\infty \beta^2} \mathrm{d}x_0, \tag{15}$$

where $\beta = \sqrt{1 - M^2}$, $\sigma = \sqrt{x^2 + \beta^2(y^2 + z^2)}$ and $g(x, K_x, k_y)$ is the transfer function between turbulent velocity and flat plate pressure jump. The far-field PSD of a flat plate interacting with turbulent gusts can be written as:[13]

$$S_{pp}(x, y, z, \omega) = \left(\frac{\omega z \rho_\infty c}{2 a_\infty \sigma^2}\right)^2 U d\pi \int_{-\infty}^{\infty} \left[\frac{\sin^2(d(k_y + \omega y/a_\infty \sigma))}{(k_y + \omega y/a_\infty \sigma)^2 \pi d}\right] |\mathcal{L}(x, K_x, k_y)|^2 \Phi_{ww}(K_x, k_y) \mathrm{d}k_y. \tag{16}$$

We can observe in equation (15) that the loading function of the flat plate is independent from the incoming turbulence spectrum. Hence, for a flat plate, the evolution of the radiated noise spectra when the integral length scale changes are only related to the changes of the turbulence spectrum, and the loading function remains identical.

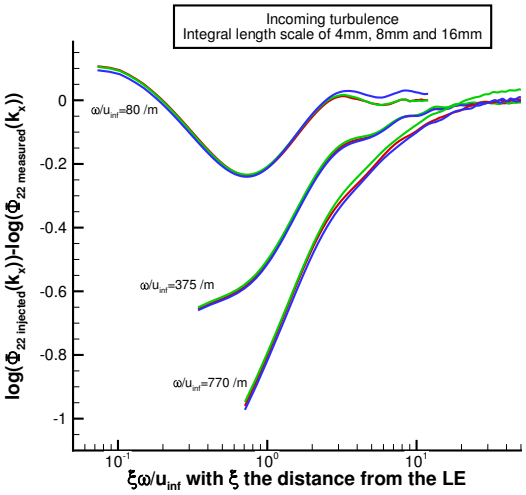

Figure 10: Distortion of the turbulence $\Phi_{22}(k_x)$ for different integral length scales.

The distortion of $\Phi_{22}(k_x)$ (Figure 10) in the vicinity of the leading edge shows that each wavenumber has the same evolution, regardless of the incoming turbulence. Hence, similary to a flat plate, the loading function can be assumed to be independent from the incoming turbulence spectrum. This behavior has been previously observed[10] by comparing the Sound Pressure Levels and directivities in the far-filed of a cambered airfoil with the Amiet model.

IV.C. Effect of the chord

The next sections are now focusing on the change in geometry of the airfoil, and its effects on the distortion of the turbulence as well as the acoustic response.

The first geometric parameter to be studied is the chord of the profile, without changing the geometry forward the location of the maximum thickness. Hence the physical dimensions of the nose radius, the location of the maximum thickness and the profile thickness remain identical. In this section, two chords are considered: 0.1 m and 0.15 m and are plotted on Figure 11. The parameters of the two profiles are written in Table 1.

It is important to note that the second profile is not equivalent to a NACA0008-92 with a chord of 0.15m, despite respecting the same thickness, nose radius and location of the maximum thickness. Indeed, the curve from leading edge to the maximum thickness location differs from a NACA0012-63 (chord=0.1m) and a NACA0008-92 (chord=0.15m).

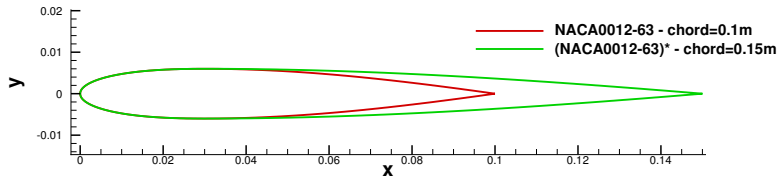

Figure 11: Profiles with different chord

Chord	Thickness (equivalent index t)	Nose radius (equivalent index I)	Location of the maximum (equivalent index m)
0.1 m	$1.2e^{-2}$ m ($t = 12$)	$R_{LE} \approx 1.59e^{-3}$ m ($I = 6$)	0.03 m ($m = 3$)
0.15 m	$1.2e^{-2}$ m ($t = 8$)	$R_{LE} \approx 1.59e^{-3}$ m ($I = 9$)	0.03 m ($m = 2$)

Table 1: Parameters of the profiles

As the two considered profiles are identical from the leading edge to the maximum thickness location, the two mean flows are very similar (Figure 12). While the mean pressure shows a difference of well under 1% in the region forward the maximum ordinate of the profiles, it should be noted that noticeable, yet small differences after $x = 0.2$m can be observed on the mean velocity in the x-direction.

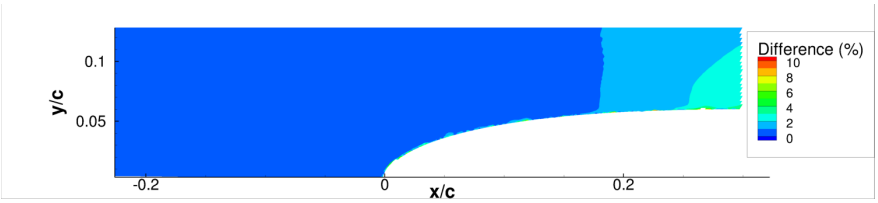

(a) u

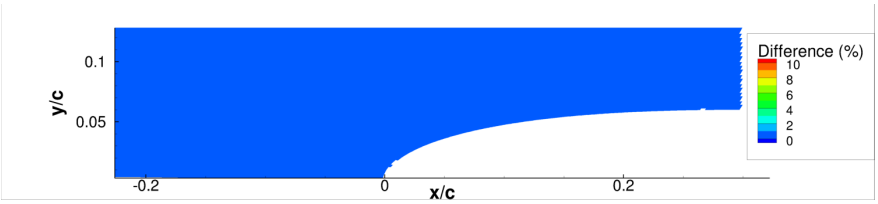

(b) p

Figure 12: Mean flow difference between the profiles with different chords.

The mean flow being very similar forward the position of the maximum thickness, the turbulence distortion on the streamline which goes to the stagnation point is unchanged, as shown on Figure 13b. The SPL, for example at 90°as plotted on Figure 13a, does not indicate differences other than those expected from the change in chord length in the Amiet model,[13] such as a shift in the lobe location.

It suggests that the turbulence distortion does not depend on the geometry aft the maximum ordinate of the profile. This result is not surprising as it has been shown that the boundary layer has a feeble effect on the interaction noise.[10,14] Hence, it supports the use of a steady Euler as a valid mean flow assumption for interaction noise investigations.

IV.D. Effect of the chordwise location of the maximum thickness

The location of the maximum thickness is now studied for three different thickness: t=6%, t=12% and t=24%. The studied positions of the maximum thickness range from 20% (m=2) to 50% (m=5) of the chord from the leading edge. The profiles for a thickness of 12% are plotted on Figure 14. One should note that the 50% location associated with a thickness of 24% have not been studied due to difficulties encountered to

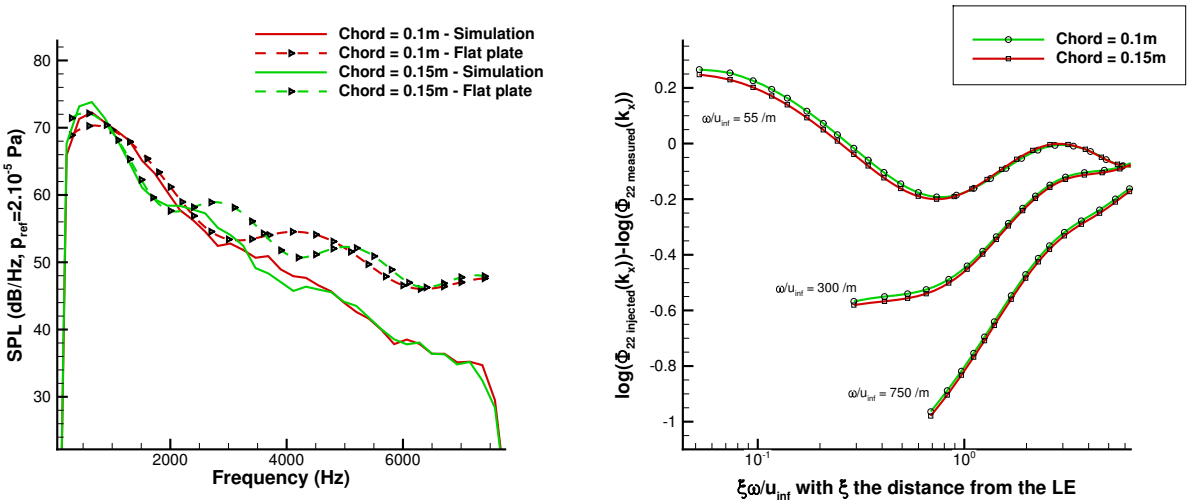

(a) Acoustic radiation at 90°and R=1.2m.

(b) Distortion of $\Phi_{22}(k_x)$.

Figure 13: Sound pressure level and distortion of the turbulence for profiles with different chords.

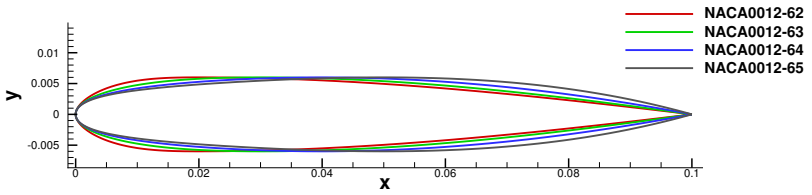

Figure 14: NACA0012-6i with i varying from 2 to 5.

obtain a correct mean flow.

For the three thickness considered, the acoustic results as well as the turbulence distortion are similar behavior, hence only the results for a thickness of 12% are plotted. The Figure 15a shows the SPL for the different locations of the maximum thickness. We can observe that the closer the maximum ordinate is to the leading edge, the larger the noise reduction occurs at high-frequency, as previously observed.[16] On the other part of the spectrum, low frequencies remain unaffected by the geometry, as the wavelengths are greater than the chord of the profile. The evolution of the distortion of $\Phi_{22}(k_x)$ indicates that the evolution of a fixed wavenumber for a case with a given m behaves similarly to a lower wavenumber for a case with a larger m (i.e. smaller slope between nose and the maximum thickness).

IV.E. Effect of the nose radius

In this section, the effect of the size of the nose radius is studied. The thickness and location of the maximum ordinate are kept identical through the different nose radii considered. Three nose radius have been studied, a nose radius from a NACA0012-63, which acts as a baseline, and then a nose radius two times smaller and two times larger than this baseline. The parameters of the profiles are written in the Table 2.

Figure 16b shows the SPL with the different nose radii. It depicts that the blunter the nose radius is, the larger the nose reduction occurs at high-frequency, as observed experimentally[15] and numerically.[16] The distortion of $\Phi_{22}(k_x)$ (Figure 16a) shows that at low frequency, despite having no impact of the radiated far-field noise (Figure 16b), the distortion differs on the closest points to the leading edge. Also, the distortion of $\Phi_{22}(k_x)$ indicates that the evolution of a fixed wavenumber for a case with a given nose radius behaves similarly to a lower wavenumber for a case with a larger nose radius (i.e. blunter leading edge).

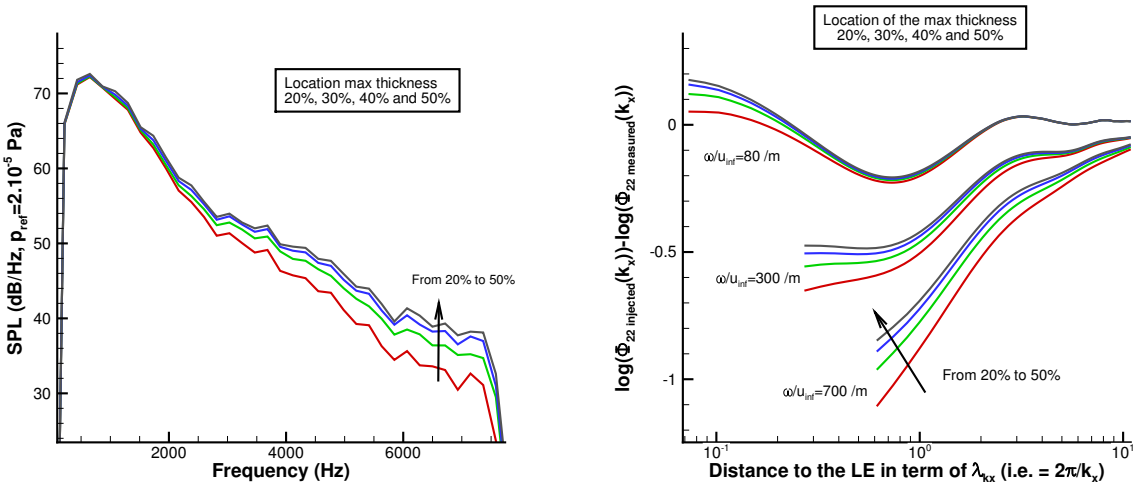

(a) SPL at 90°and R=1.2m above the airfoil.

(b) Distortion of $\Phi_{22}(k_x)$.

Figure 15: Distortion of $\Phi_{22}(k_x)$ and SPL on a NACA0012 for different locations of maximum ordinate.

Nose radius (equivalent index I)
$R_{LE} \approx 0.79e^{-3}$ m $(I \approx 4.24)$
$R_{LE} \approx 1.59e^{-3}$ m $(I = 6)$
$R_{LE} \approx 3.17e^{-3}$ m $(I \approx 8.48)$

Table 2: Parameters of the profiles

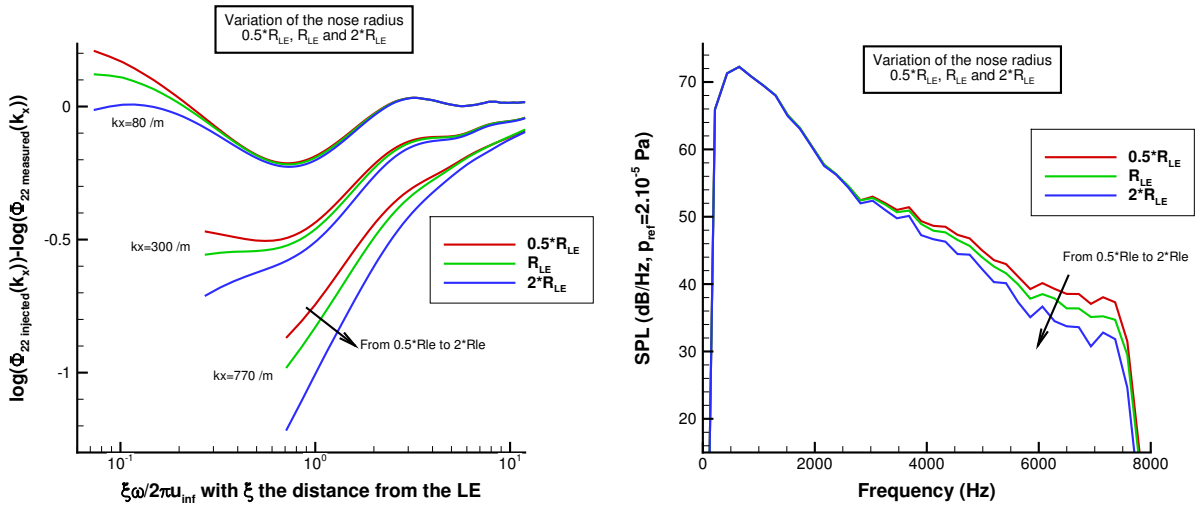

(a) Distortion of $\Phi_{22}(k_x)$.

(b) SPL at 90°and R=1.2m above the airfoil

Figure 16: Distortion of $\Phi_{22}(k_x)$ and SPL for different nose radii.

IV.F. Effect of the thickness

The effect of the maximum thickness is now studied, considering three different thickness (6%, 12% and 24%), each investigated for two fixed nose radius size. Hence, 6 profiles have been considered, with a

thickness of 6%, 12% to 24% with first the nose radius of a NACA0006-63, and then with the nose radius of a NACA0012-63. The Table 3 details the parameters of the profiles.

Nose radius (equivalent index I)	Thickness (equivalent index t)
$R_{LE} \approx 3.97e^{-4}$ m (I = 6)	$0.6e^{-2}$ m (t = 6)
$R_{LE} \approx 3.97e^{-4}$ m (I = 3)	$1.2e^{-2}$ m (t = 12)
$R_{LE} \approx 3.97e^{-4}$ m (I = 1.5)	$2.4e^{-2}$ m (t = 24)
$R_{LE} \approx 1.59e^{-3}$ m (I = 12)	$0.6e^{-2}$ m (t = 6)
$R_{LE} \approx 1.59e^{-3}$ m (I = 6)	$1.2e^{-2}$ m (t = 12)
$R_{LE} \approx 1.59e^{-3}$ m (I = 3)	$2.4e^{-2}$ m (t = 24)

Table 3: Parameters of the profiles

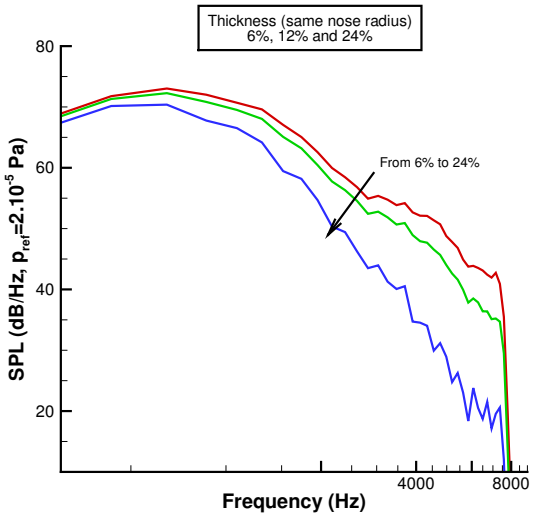

Figure 17: SPL at 90°and R=1.2m above the airfoil for three different thickness with a nose radius of a NACA0012-63.

The distortion of $\Phi_{22}(k_x)$ as well as the SPL considering the two different nose radii show similar trends, thus only the results with a nose radius of a NACA0012-63 are plotted. As previously observed,[15,16] the SPL on Figure 17 shows a large reduction in amplitude as the frequencies and the thickness increase. Regarding the distortion of $\Phi_{22}(k_x)$, the thickness t seems to be an important factor. Indeed, a partial similarity of the evolution of the distortion can be obtained (Figure 18) with the parameter ft/u_∞, yet the curves do not collapse perfectly. It suggests that the high wavenumbers of the thin airfoil behave similarly to the lower wavenumbers of a thick airfoil.

IV.G. Effect of the curvature forward the maximum thickness

The nose radius, thickness and chordwise location of the maximum thickness all have an effect on the distortion of the turbulence. To understand the effect of the curvature from the the leading edge to the maximum thickness, three profiles have been studied. These profiles have the same nose radius, thickness and location of the maximum thickness. To construct these profiles, a NACA0012-63 with a chord of c=0.1m is chosen as a baseline. Then, for the two other profiles, only the part forward the maximum thickness has been modified for the three profiles, hence they keep the part aft the maximum thickness and by extension the same chord. To obtain the new curvatures while conserving the same physical dimensions of the nose radius, thickness and location of the maximum thickness, a NACA0008-92 with a chord of c=0.15m and a NACA0016-4.54 with a chord of c=0.075m are used. The resulting profiles are plotted in Figure 19 and their

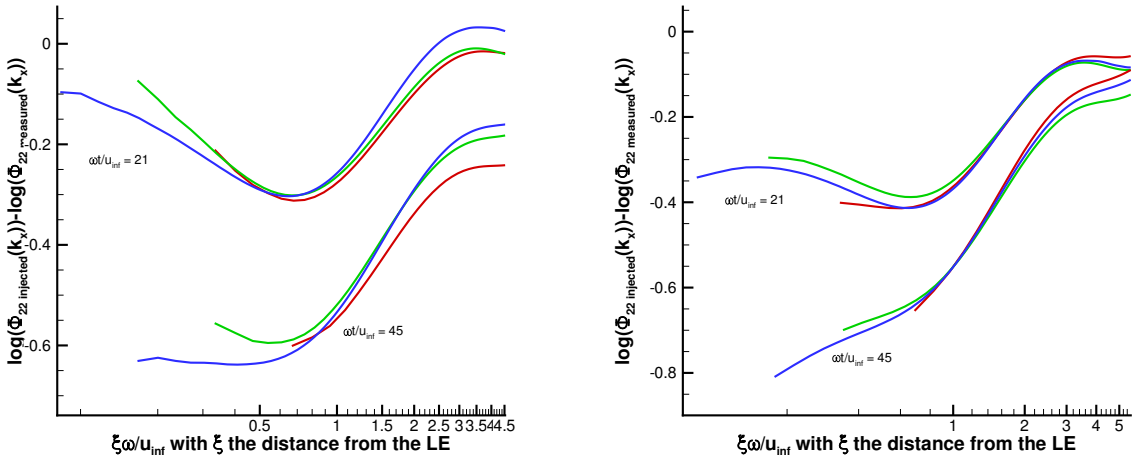

(a) Nose radius of a NACA0006-63.

(b) Nose radius of a NACA0012-63.

Figure 18: Distortion of $\Phi_{22}(k_x)$ for different thickness.

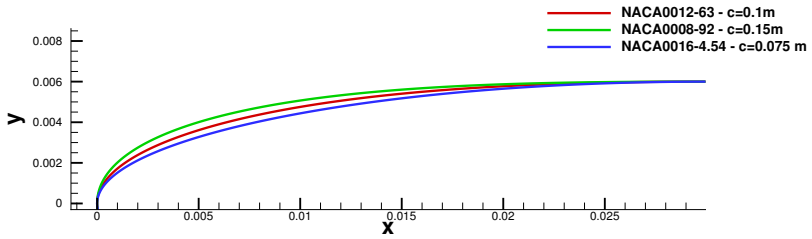

Figure 19: Profiles used to study the effect of the curvature forward the maximum thickness.

parameters are listed in Table 4.

	Foward the maximum thickness		Aft the maximum thickness	
	4-digit NACA	Chord	4-digit NACA	Chord
Profile 1	NACA0012-63	c = 0.1 m	NACA0012-63	c = 0.1 m
Profile 2	NACA0008-92	c = 0.15 m		
Profile 3	NACA0016-4.54	c = 0.075 m		

Table 4: Parameters of the profiles

Despite having the same nose radius, thickness and location of the maximum thickness, the SPL, plotted in Figure 20a, shows a noise reduction at high frequencies when the bluntness of the profile aft the nose is more important. This result is confirmed by looking at the distortion of wavenumber velocity spectra $\Phi_{22}(k_x)$, plotted in Figure 20b. This result suggests that the nose radius, thickness and chordwise location of the maximum thickness are not sufficient parameters to describe the geometry regarding the distortion of the turbulence.

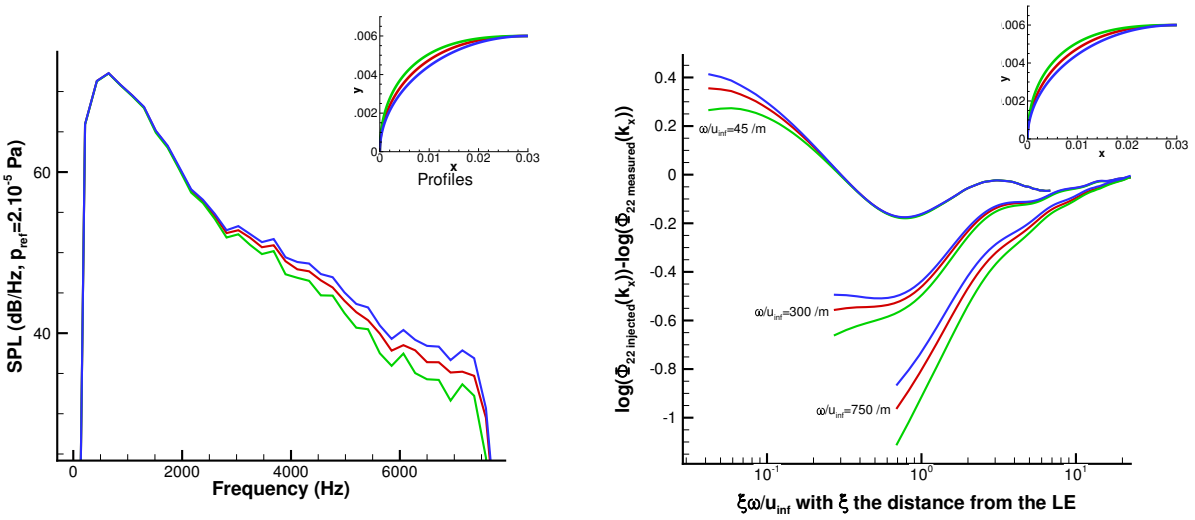

(a) SPL (b)

Figure 20: Distortion of $\Phi_{22}(k_x)$ for different curves forward the maximum thickness.

V. Conclusion

A method to inject synthetic turbulence in a computational domain using localized vorticity sources has been extended to generate two-component turbulence. This method has the advantages of being easy to implement and has no influence on the parallelization of the solver, whilst the turbulence generated is frozen. The method has been validated in a free-field configuration considering a uniform mean flow and using a CAA method solving the linearized Euler equations. Then, using this method to synthesize a one- and two-component turbulence, the distortion of the turbulence in the vicinity of the leading edge of a symmetric NACA profile is studied. The distortion of the incoming turbulence by the mean flow close to the leading edge is believed to play an important role in the interaction noise. The results indicate first that no distortion is occurring far from the profile. Then, at a threshold distance common to all frequencies, around half a chord upstream the airfoil, the levels of the upwash velocity fluctuations starts to decrease uniformly, independently of the wavenumber. This decay is however inverted for low frequencies after a second threshold distance, much closer to the leading edge, which is wavenumber dependent (i.e. proportional to the hydrodynamic wavelength). This augmentation becomes however less important as the frequency increases, to become inexistent at high frequencies. One can note that at low frequencies, really close to the stagnation region, the wavenumber spectrum of the fluctuating velocity component normal to the chord is higher than the levels of the turbulence injected initially. Nevertheless these higher levels do not lead to an increase of the radiated noise at low frequencies when the far-field spectrum is compared to a flat plate where no turbulence distortion occurs. Afterwards, a parametric study has been performed to investigate some characteristics of the turbulence distortion. The variation of the mean flow velocity showed that the first (wavenumber-independent) and second (wavenumber-dependent) threshold distances are reduced as the mean flow velocity is increased. Yet, it should be noted that at the considered velocities, the compressibility effects are small. Otherwise, at a given wavenumber, despite a different second threshold distance location, the evolution of the turbulence behaves similarly for all the velocities. The effect of the incoming turbulence spectrum is then investigated to suggest that the distortion and thus the airfoil response function are independent from the incoming turbulence. Then, a NACA0012-63 profile has been modified aft the position of the maximum thickness, to consider a longer chord. The geometry forward the maximum thickness being identical, the mean flow showed very little differences in this region, resulting in no differences on the turbulence distortion. As a result, the radiated far-field noise does not indicate differences other than those expected from the change in chord length. This result confirms that the distortion does not depend on the geometry aft the maximum ordinate, which also support that the boundary layer has a feeble effect on the interaction noise. A change in the position of the maximum thickness as well as the size of the

nose radius indicate that blunter geometries reduce interaction noise at high frequencies. Moreover, it is shown that the thickness is an important parameter as a partial similarity of the distortion can be obtained with the parameter ft/u_∞. Finally, by modifying the curvature of the part foward the maximum thickness, while conserving the same physical nose radius, thickness and position of the maximum thickness, it can be concluded that these parameters alone are not sufficient to fully account for the distortion of the turbulence, and hence the radiated noise.

Acknowledgements

The work was funded by Innovate UK, HARMONY Programme (GA n° 101367). Rolls-Royce Plc is also acknowledged for the financial and technical support given.

The authors would like to thank the DLR for providing the CAA solver PIANO. The authors acknowledge the use of the IRIDIS High Performance Computing Facility, and associated support services at the University of Southampton, in the completion of this work.

References

[1]P. R. Gliebe and B. A. Janardan. Ultra-high bypass engine aeroacoustic study. Technical report, NASA, 2003.

[2]R. Kraichnan. Diffusion by a random velocity field. *Physics of Fluids*, 13(1):22–31, 1970.

[3]R. Ewert and W. Schröder. Acoustic perturbation equations based on flow decomposition via source filtering. *J. Comput. Phys.*, 188:365–398, 2003.

[4]R. Ewert. Broadband slat noise prediction based on CAA and stochastic sound sources from a fast Random Particle-Mesh (RPM) method. *Computers and Fluids*, 37:369–387, 2008.

[5]M. Dieste and G. Gabard. Broadband fan interaction noise using synthetic inhomogeneous non-stationary turbulence. In *17th AIAA/CEAS Aeroacoustics Conference*, number AIAA-2009-3267, 2011.

[6]M. Dieste and G. Gabard. Random particle methods applied to broadband fan interaction noise. *Journal of Computational Physics*, 231:8133–8151, 2012.

[7]N. Jarrin, S. Benhamadouche, D. Laurence, and R. Prosser. A synthetic-eddy method for generating inflow conditions for large-eddy simulations. *International Journal of Heat and Fluid Flow*, 27:585–593, 2006.

[8]N. Jarrin, J-C. Uribe, R. Prosser, and D. Laurence. *Advances in Hybrid RANS-LES Modelling*, volume 97, chapter Synthetic Inflow Boundary Conditions for Wall Bounded Flows, pages 77–86. Springer, 2008.

[9]N. Jarrin, R. Prosser, J-C. Uribe, S. Benhamadouche, and D. Laurence. Reconstruction of turbulent fluctuations for hybrid rans/les simulations using a synthetic-eddy method. *International Journal of Heat and Fluid Flow*, 30:435–442, 2009.

[10]Thomas Hainaut, Gwenael Gabard, and Vincent Clair. Caa study of airfoil broadband interaction noise using stochastic turbulent vorticity sources¡br /¿. In *AIAA Aviation*, pages –. American Institute of Aeronautics and Astronautics, June 2015.

[11]M. Dieste. *Random-Vortex-Particle Methods Applied to Broadband Fan Interaction Noise*. PhD thesis, University of Southampton, 2011.

[12]V. Clair. *Calcul numrique de la rponse acoustique d'un aubage soumis un sillage turbulent*. PhD thesis, Universit Claude Bernard Lyon 1, 2013.

[13]R.K. Amiet. Acoustic radiation from an airfoil in turbulent stream. *Journal of Sound and Vibration*, 41(4):407–420, 1975.

[14]J. Gill. *Broadband Noise Generation of a Contra-Rotating Open Rotor Blade*. PhD thesis, Airbus Noise Technology Centre, University of Southampton, 2015.

[15]Chaitanya Paruchuri, James R. Gill, Narayanan Subramanian, Phillip Joseph, Christina Vanderwel, Xin Zhang, and Bharathram Ganapathisubramani. Aerofoil geometry effects on turbulence interaction noise. In *AIAA Aviation*, pages –. American Institute of Aeronautics and Astronautics, June 2015.

[16]James Gill, X. Zhang, and P. Joseph. Symmetric airfoil geometry effects on leading edge noise. *Journal of acoustical society of America*, 134(4), 2013.

[17]L. Santana, C. Schram, and W. Desmet. Airfoil noise prediction from 2d3c piv data. In *21st AIAA/CEAS Aeroacoustics Conference*, 2015.

[18]J. Hunt. A theory of turbulent flow round two-dimensional bluff bodies. *Journal of Fluid Mechanics*, 61:625–706, 1973.

[19]G. K. Batchelor and I. Proudman. The effect of rapid distortion of a fluid in turbulent motion. *The Quarterly Journal of Mechanics and Applied Mathematics*, 7(1):83–103, 1954.

[20]J. Christophe. *Application of Hybrid Methods to High Frequency Aeroacoustics*. PhD thesis, von Karman Institute for Fluid Dynamics, 2011.

[21]S. Glegg and W. Devenport. Turbulence modeling for rotor stator interaction noise. In *16th AIAA/CEAS Aeroacoustics Conference*, number AIAA-2010-3745, 2010.

[22]Peter D. Lysak, Dean E. Capone, and Michael L. Jonson. Prediction of high frequency gust response with airfoil thickness effects. *Journal of Fluids and Structures*, 39:258–274, May 2013.

[23]M. Howe. Unsteady lift and sound produced by an airfoil in a turbulent boundary layer. *Journal of Fluids and Structures*, 15(2):207–225, February 2001.

[24]Daehwan Kim, Gwang-Se Lee, and Cheolung Cheong. Inflow broadband noise from an isolated symmetric airfoil interacting with incident turbulence. *Journal of Fluids and Structures*, 55:428–450, May 2015.

[25]B.-T. Chu and L. Kovásznay. Non-linear interactions in a viscous heat-conducting compressible gas. *Journal of Fluid Mechanics*, 3(5):494–514, 1958.

[26]C. Tam and J. Webb. Dispersion-Relation-Preserving finite difference schemes for computational acoustics. *Journal of Computational Physics*, 107:262–281, 1993.

[27]J.M. Nichols, C.C. Olson, J.V. Michalowicz, and F. Bucholtz. A simple algorithm for generating spectrally colored, non-gaussian signals. *Probabilistic Engineering Mechanics*, 25:315–322, 2010.

[28]F. Elliott, D. Horntrop, and A. Majda. A fourier-wavelet monte carlo method for fractal random fields. *Journal of Computational Physics*, 132:384–408, 1997.

[29]G. Gabard. Noise sources for duct acoustics simulations: Broadband noise and tones. *AIAA Journal*, 52:1994–2006, 2014.

[30]Ira H. Abbott and A.E. von Doenhoff. *Theory of Wing Sections: Including a Summary of Airfoil Data*. Dover Publications, 1959.

[31]David P. Lockard. An efficient, two-dimensional implementation of the Ffowcs-Williams and Hawkings equation. *Journal of Sound and Vibration*, 229(4):897–911, 2000.

[32]David P. Lockard. A comparison of Ffowcs Williams-Hawkings solvers for airframe noise applications. In *8th AIAA/CEAS Aeroacoustics Conference*, number AIAA-2002-2580, 2002.